



Tungsten/bismuth – based catalysts for the degradation of 5-fluorouracil cytostatic drug in water by solar-LED photocatalysis

Velma Beri Kimbi Yaah^{a,b,*}, L.M. Pastrana-Martínez^a, F.J. Maldonado-Hódar^a, S. Morales-Torres^{a,**}

^a NanoTech – Nanomaterials and Sustainable Chemical Technologies, Department of Inorganic Chemistry, Faculty of Sciences, University of Granada, Avda. Fuente Nueva s/n, Granada ES18071, Spain

^b Environmental and Chemical Engineering (ECE), Faculty of Technology, University of Oulu, P.O. Box 4300, Oulu FI-90014, Finland

ARTICLE INFO

Keywords:

5-Fluorouracil
Photocatalysis
Bi₂O₃
Bi₂WO₆
WO₃
Water treatment
Solar-LED
Hydrothermal

ABSTRACT

A new series of photocatalysts, including WO₃, Bi₂O₃ and Bi₂WO₆, were prepared for the photo-oxidation of 5-Fluorouracil (5-FU) in water, as a model of cytostatic drug, under solar-LED irradiation. The materials were hydrothermally prepared under the same experimental conditions, and the effect of incorporating an activated carbon during the synthesis and further post-treatments in air or nitrogen atmosphere were investigated. All photocatalysts were thoroughly characterized by complementary techniques analyzing their morphologies and physicochemical properties, which differed based on the type of semiconductor used. In general, the addition of carbon led to an increased porosity ($S_{\text{BET}} = 20\text{--}50 \text{ m}^2/\text{g}$), a reduced band gap ($E_g = 2.7\text{--}2.9 \text{ eV}$) and a lower crystallite size compared to the original semiconductor. The photocatalytic performance of the materials depended also on the thermal post-treatment, while N₂ treatment improved the efficiency of Bi-carbon composites, the air treatment did not influence the pure semiconductors. The 5-FU degradation varied as WO₃ (10 %) < Bi₂WO₆ (36 %) < Bi₂O₃ (68 %) after 100 min under solar-LED irradiation, while their corresponding carbon-metal composites always improved the performance. In particular, the conversion of 5-FU after 100 min of reaction was 64 % and 84 % for Bi₂WO₆-3C and Bi₂WO₆-3C-n, while the carbon-Bi₂O₃ composite achieved total photodegradation of 5-FU ($k_{\text{app}} = 43.89 \times 10^{-3} \text{ min}^{-1}$) after ~100 min of reaction and under solar-LED irradiation.

1. Introduction

Effluents from pharmaceutical industries, hospitals and municipal wastewater treatment plants (WWTPs) contain organic compounds that end up in the aquatic environment. One of such pharmaceuticals are the cytostatic drugs used to inhibit or completely block the growth of cancerous cells, and trigger cell death when possible (Crowley et al., 2016; Jureczko and Kalka, 2020). Different studies have reported the occurrence of cytostatic drugs at concentrations between ng L⁻¹ to µg L⁻¹ in natural waters in Europe (Feng et al., 2015; Ganzenko et al., 2018). Their presence in aquatic environments possesses negative genotoxic, teratogenic, carcinogenic,

* Corresponding author at: NanoTech – Nanomaterials and Sustainable Chemical Technologies, Department of Inorganic Chemistry, Faculty of Sciences, University of Granada, Avda. Fuente Nueva s/n, Granada ES18071, Spain.

** Corresponding author.

E-mail addresses: velma.kimbiyaah@oulu.fi (V.B.K. Yaah), semoto@ugr.es (S. Morales-Torres).

<https://doi.org/10.1016/j.eti.2025.104148>

Received 30 December 2024; Received in revised form 2 March 2025; Accepted 11 March 2025

Available online 17 March 2025

2352-1864/© 2025 The Author(s). Published by Elsevier B.V. This is an open access article under the CC BY license (<http://creativecommons.org/licenses/by/4.0/>).

cytotoxic and mutagenic effects on aquatic organisms and human health as well (Lutterbeck et al., 2016; Pérez-Molina et al., 2023). They are not easily removed by natural attenuation in the environment, neither are they effectively treated by the conventional methods used in WWTPs. As a result, different methods are sort for their possible treatment from water.

Advanced oxidation processes have been studied to potentially degrade persistent and recalcitrant organic pollutants. Among them, the development of efficient visible-light active photocatalysts for the treatment of resistant pharmaceuticals has been one of the important aspects of photocatalysis research. Recently, bismuth-based photocatalysts have been reported to be interesting alternatives to TiO_2 due to their good visible light absorption properties due to narrow band gaps (Muruganandham et al., 2012). Finding simple and non-toxic precursors, and routes for the synthesis of these photocatalysts with different structures and morphologies is vital in this regard. Tungsten and bismuth oxide photocatalysts have also garnered interest due to their wide radiation range, in particular, under solar or visible radiation, band gap values between 2.7 and 3.0 eV, the easy lab-scale synthesis and environmentally benign nature. However, the slow charge transfers and fast recombination of photogenerated electron-hole pairs during photocatalytic degradation using semiconductors based on pure metal oxides are still a challenge (Bayahia, 2022). Furthermore, these pure materials are also known to have a low specific surface area and porosity, which adversely affect to their photocatalytic performance.

Carbon materials have the ability to delocalize charge carriers of semiconductors hence, reducing the electron hole recombination rate, extending the photoactivity to longer light wavelengths and enhancing the porosity (Bu et al., 2023; Morales-Torres et al., 2012; Pastrana-Martínez et al., 2012). This is due to its ability to delocalize charge carriers in the π -electron density of their graphitic layers. Therefore, incorporating carbon in metal oxide semiconductors, as dopants or additives (Raza and Ahmad, 2022), is a strategy to obtain high photoconversion efficiencies in the degradation of contaminants (Gomis-Berenguer et al., 2019).

In this work, tungsten/bismuth-based photocatalysts were synthesized by a hydrothermal method maintaining time and temperature, further thermally treated in air or nitrogen flow. These materials were also used to prepare carbon-semiconductor oxide composites to be applied as photocatalysts for the photodegradation of 5-fluorouracil (5-FU) under solar-LED irradiation and compared with the corresponding bare metal oxides. The main aim of this work is to study the influence of various post-treatments on hydrothermally synthesized tungsten/bismuth-based photocatalysts, physical, chemical and optical properties being analyzed through different characterization techniques and correlated with their photocatalytic activity for the removal of a 5-FU cytostatic drug. In addition, an activated carbon (AC) from spruce wood was added during the hydrothermal synthesis to lead metal-carbon composites to enhance their properties and activity under solar-LED irradiation. Mane et al., (2024a) published an extensive review on Bi_2O_3 nanomaterials for photocatalytic and antibacterial application. They also modified Bi_2O_3 with other materials such as Fe, Zn and graphene oxide, but most of the applications were limited to the removal of conventional dyes in water (Mane et al., 2023; V. A. Mane et al., 2024c; Vijay A. Mane et al., 2024b). This shows that the catalysts synthesized in this work, active under solar-LED irradiation, have been reported less so far in the removal of cytostatic drugs.

2. Materials and methods

2.1. Synthesis of materials

The materials studied in this work, in particular bismuth oxide (Bi_2O_3), bismuth tungstate (Bi_2WO_6) and tungsten oxide (WO_3), were synthesized adapting the methods described in previous works. For Bi_2O_3 , 1.2 g of $\text{BiNO}_3 \cdot 5\text{H}_2\text{O}$ ($\geq 98\%$, Alfa Aesar) was dissolved in 1 mL of HNO_3 (68%, VWR Chemicals) and 50 mL of deionized water, stirred at 250 rpm for an hour, while 0.90 g of anhydrous oxalic acid (98%, Thermo scientific) was dissolved in 50 mL of water. Then, both solutions were mixed and transferred to an autoclave, which was placed in a furnace at 150 °C for 12 h (Muruganandham et al., 2012). To prepare WO_3 , 3.2 g of $\text{Na}_2\text{WO}_4 \cdot 2\text{H}_2\text{O}$ (99%, Acros Organics Chemicals) and 0.10 g of pure NaCl were dissolved in 60 mL of deionized water and stirred for 1 h. Then, 15 mL of HCl (37%, VWR Chemicals) was added dropwise for 30 min. After that, the resulting solution was transferred to an autoclave, which was heated at similar conditions (150 °C, 12 h) (Bayahia, 2022). For Bi_2WO_6 , 5.0 g of $\text{BiNO}_3 \cdot 5\text{H}_2\text{O}$ was dissolved in 10 mL of acetic acid (99.8%, Sigma Aldrich) and 1.2 g of $\text{Na}_2\text{WO}_4 \cdot 2\text{H}_2\text{O}$ was dissolved in 90 mL of deionized water and then, both solutions were mixed and stirred for 1 h, transferred to an autoclave and heated at 150 °C for 12 h (Gomis-Berenguer et al., 2019). In all cases, as-prepared metal oxides were washed repeatedly with deionized water and ethanol, and then dried at 80 °C overnight. Carbon-W/Bi composites were prepared under a similar methodology by adding a 3.0 wt% of AC during the metal oxide synthesis. This AC was previously prepared by physical activation with CO_2 at 800 °C from spruce wood following a similar procedure to that described elsewhere (Regadera-Macías et al., 2024). Further thermal post-treatments were done at 300 °C with a 5 °C min^{-1} heating rate under N_2 flow for 2 h in a horizontal oven (Forns Hobersal), or under static air atmosphere at 450 °C for 5 h in a muffle furnace (Nabertherm L 9/11/B510). The materials will be labelled in the text indicating their chemical formula and by adding “3 C” for the carbon composite, while “a” or “n” refers to the thermal post-treatment done at 450 °C in air or at 300 °C in N_2 , respectively. It is worthwhile noting that Bi-carbon composites presented a complete burnout of the carbon during the thermal treatment in air, nitrogen treatments being preferred.

2.2. Characterization techniques

The physico-chemical properties of the prepared materials were characterized using different techniques. The thermogravimetric (TG) analysis (heating up to 800 °C under air flow at 20 °C min^{-1}) was carried out using a SHIMADZU TGA-50H thermobalance until constant weight. X-ray diffraction (XRD) patterns were obtained using a Philips PW 1710 diffractometer equipped with a $\text{CuK}\alpha$ radiation and a nickel filter that removes $\kappa\beta$ radiation. The N_2 adsorption-desorption isotherms were obtained at -196 °C using a

Quantachrome Quadrasorb SI equipment. Previously, the samples were degassed overnight at 110 °C under high vacuum (10^{-4} mbar). The specific surface area (S_{BET}) was calculated from the Brunauer–Emmett–Teller (BET) equation, while the total pore volume (V_{pore}) was estimated from the N_2 volume adsorbed at a relative pressure (P/P_0) of 0.95 (Brunauer et al., 1938; Sing, 1985). The pore size distribution (PSD), including the mean pore size (d_{pore}), was analyzed using Barret–Joyner–Halenda (BJH) method (Barrett et al., 1951). The morphology of the synthesized materials was analyzed by an ultra-high resolution scanning electron microscopy (FE-SEM) using a JSM-IT800 SHL microscope from JEOL LTS equipped with an in-lens Schottky Plus field emission electron gun (FEG), an electron optical NEO engine and a fully embedded energy dispersive X-Ray spectrometer (EDS). A UV-Vis spectrophotometer CARY 5E from VARIAN equipped with a diffuse reflectance accessory (DRA) was used to study the optical properties of materials, and their corresponding band gaps were determined from the corresponding Tauc's plots. Combining the reflectance data and the absorption coefficient, the Eq. 1 below based on the Kubelka-Munk theory is used to interpret the spectra. In this equation, E_g is the band gap to be calculated (eV), A is the proportionality constant, α is the absorption coefficient, h is the Planck constant, ν is the frequency of the light radiation and n is the transition (Ahmad et al., 2024).

$$ah\nu = A(h\nu - E_g)^n \quad (1)$$

Photoluminescence (PL) spectra of materials were recorded using a HORIBA QuantaMaster-8000 spectrofluorometer with an excitation wavelength of 360 nm. X-ray photoelectron spectroscopy (XPS) analysis was performed using a Physical Electronics VersaProbe II apparatus with a hemispherical electron analyzer and a MgK X-ray source ($h\nu = 1486.6$ eV) working at 1.3 eV and 20 mA. Survey and multi-region spectra were recorded at the C1s, O1s, Bi4f and W4f photoelectron peaks.

2.3. Photocatalytic reactions

The photocatalytic activity of the prepared materials was studied in the degradation of 5-Fu in aqueous solution under solar-LED irradiation at room temperature. The photocatalytic experiments were carried out in a glass reactor containing 100 mL of 5-FU (5 mg L^{-1}) and a catalyst loading of 1 g L^{-1} . The concentration of 5-FU was monitored at different time intervals at wavelength of 265.5 nm using a Shimadzu UV-2600 UV VIS spectrophotometer. The activity of the materials after the hydrothermal synthesis was also tested to better understand the effect of the post-treatments on their performance.

3. Results and discussion

3.1. Materials characterization

Thermogravimetric and differential thermogravimetric analysis (TG/DTG) was carried out to ascertain the thermal stability of the photocatalysts and to estimate the carbon content incorporated to the carbon-metal composites by burning. Fig. 1a shows, as an example, the TG and DTG profiles recorded for the as prepared Bi_2WO_6 -3C composite with increasing the temperature at $10 \text{ }^\circ\text{C min}^{-1}$ in air flow up to 700 °C. Un-doped Bi_2WO_6 was used as reference, under identical experimental conditions. The photocatalysts showed a good thermal stability up to about 400 °C, in which no mass variation was recorded. In the case of Bi_2WO_6 , the total weight loss (WL) was about 2 wt% with a main process at 325 °C corresponding to the rest of unreacted precursors (Majumdar et al., 2014; Narayanan and Mandal, 2023). For the Bi_2WO_6 -3C composite, the total WL is 4.8 wt%. At low temperature, the DTG peak around 150 °C is associated to dehydration processes, followed by two thermal decomposition processes. The first one observed at ~ 345 °C is in good agreement with the band observed for pure Bi_2WO_6 , while the new WL at ~ 415 °C is probably therefore due to the carbon phase

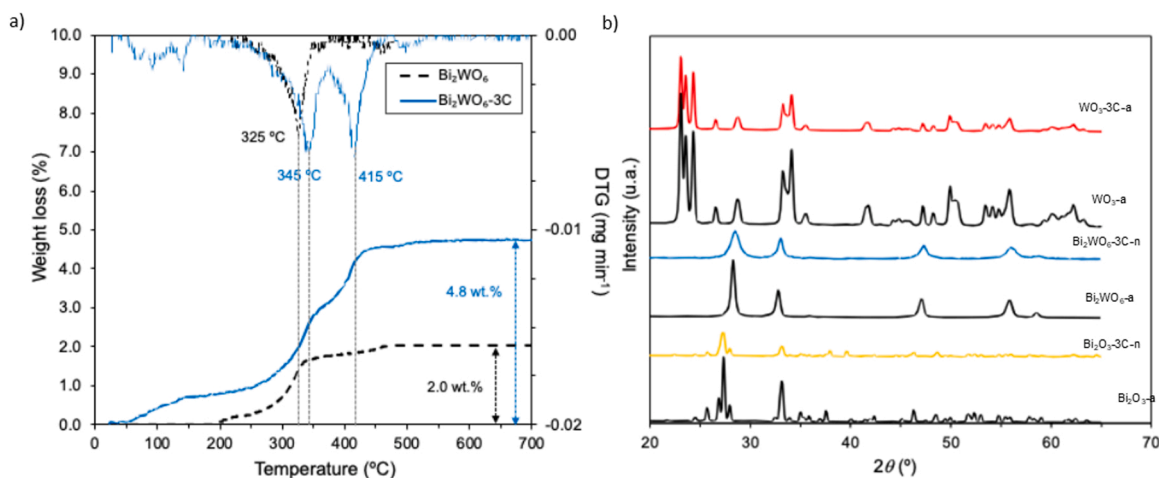


Fig. 1. (a) TG and DTG profiles for neat Bi_2WO_6 and Bi_2WO_6 -3C under air atmosphere, and (b) XRD patterns for the neat metal oxides and their metal-carbon composites.

combustion incorporated in the composite. No significant WL occurs from this temperature range. The determined carbon content was around 2.8 wt%, in agreement with the theoretical carbon amount (3 wt%). In both materials, there is almost no weight loss after about 415 °C, the photocatalysts being quite stable at high temperatures.

The crystallinity of the metal oxide photocatalysts and their composites was studied by XRD, the corresponding patterns being similar enough between each series of materials (Fig. 1b). No peaks associated to the carbon component or new crystalline phases induced by the interaction between carbon and metallic phases during thermal treatments, were observed, however, the wider and less intense peaks in the composite denotes a smaller crystallinity. The XRD pattern of WO₃ and WO₃-3C treated with air shows peaks that correspond to the monoclinic WO₃ phase. The diffraction peaks around 2θ= 23.0°, 23.2°, 24.3°, 28.8°, 35.7° correspond to the (002), (020), (200), (112) and (220) planes, while the peaks around 50.0°, 54.8°, 55.1°, 63.0° align with the (202), (222), (113) and (133) planes, respectively (JCPDS 71–2141) (Priya et al., 2016). This shows that the hydrothermal synthesis and the subsequent air treatment produces monoclinic phase WO₃ (Balzer et al., 2014; J. Ma et al., 2022; Wang et al., 2019; Yang et al., 2022).

The XRD peaks of Bi₂WO₆ and Bi₂WO₆-3C-n are attributed well to the orthorhombic Bi₂WO₆ (JCPDS 39–0256) (Chen et al., 2023). Four main peaks were obtained at 2θ= 28.1°, 32.6°, 46.8° and 58° corresponding to the (131), (200), (202) and (262) planes (Gui and Zhang, 2011; Rhoomi et al., 2024). In the XRD pattern of Bi₂O₃ and Bi₂O₃-3C, the main peaks were observed at 26.9° (112), 33.0° (012), 25.7° (002), 27.4° (121) and 46.3° (041) corresponding to the monoclinic α-Bi₂O₃ phase (JCPDS 01–071–2274) (Karen et al., 2021). Based on XRD results, the crystallite size (d_{crystal}) of the materials was calculated by the Scherrer equation and summarized in Table 1. As note, a decrease in crystallite sizes was observed when carbon was added to materials, especially in the case of Bi₂WO₆ (e.g., 21.6 and 8.6 for Bi₂WO₆-a and Bi₂WO₆-3C-n, respectively). However, the crystallite size was instead increased for WO₃-3C-a compared to WO₃-a. This fact could be based on that the WO₃-3C material presented were further treated in air at 450 °C, while nitrogen was used in Bi-3C-based materials were carried out at 300 °C. Additional crystallographic parameters, such as dislocation density, microstrain and stacking faults are presented in Table S1, Supplementary Material. It is observed that as the crystallite size of the materials decreases, the dislocation density, stacking fault and microstrain increase. Considering the TG results previously commented, the carbon phase could be burned by the air treatment at 450 °C generating hot spot along the sample thus increasing sintering regarding pure WO₃.

The morphology of the materials is shown in Fig. 2 and Figure S1, Supplementary Material. In the case of Bi₂WO₆, elongated nanoparticles are grouped forming microspheres, sometimes defined as flower-like particles, with sizes ranging 3–9 μm (Fig. 2a and b). When carbon was added during the hydrothermal synthesis, several changes were produced in the material surface. The nanoparticle size decreases regarding Bi₂WO₆ and their aggrupation in spheres avoided, now being placed as coating of the carbon grains added to the starting synthesis suspension (Fig. 2c and d). These observations are in agreement with those reported in literature (Gomis-Berenguer et al., 2019; Murcia-López et al., 2013). Similarly, Bi₂O₃ was composed by worm-like structures with an average length of about 1 μm (Fig. 2e), with the addition of carbon in the corresponding composite (Fig. 2f) a more heterogenous distribution of Bi₂O₃ nanoparticles coating large carbon particles is favoured. An intimate contact between the inorganic and carbon phases being always established. The synthesized WO₃ showed tiny regular and uniform nanocubes with smooth surfaces (Fig. 2g). These nanocubes seem to overlap each other forming self-assembled aggregates. This is a typical of monoclinic hydrothermally synthesized WO₃ (Wang et al., 2019). In the case of the WO₃-3C composite (Fig. 2g and Fig. S1), less uniform nanocube structures are formed and their surface seems to be less smooth compared to pure WO₃. Nevertheless, EDX analysis confirm that WO₃ is ubiquitously distributed. As commented, the air thermal treatment could remove an important part of the carbon phase, thus, the contact between the carbon grains and WO₃ nanocubes seem to be worse than in the other cases.

The N₂-adsorption-desorption isotherms and PSDs obtained by applying BJH to the isotherm data of the photocatalysts are shown in Fig. 3a and b, respectively. In general, all the materials showed isotherms classified as type II in agreement with IUPAC classification and typical for low porous materials (Pérez-Molina et al., 2023; Thommes et al., 2015). At relative pressures (P/P₀) of ~0.4–1.0, a hysteresis loop of type H3 is always observed due to mesoporosity between particles in non-rigid aggregates of plate-like particles, but also can be suggested the presence of macropores (Thommes et al., 2015) in agreement with the SEM observations. However, the N₂ adsorption at low P/P₀ was very low (Fig. 3a), which is indicative to the absence of micropores. In general, the porosity of the samples was enhanced by the addition of carbon in the composite, especially for Bi₂WO₆-3C and WO₃-3C. In fact, the BET surface areas (S_{BET}) of the photocatalysts were increased by about four folds for WO₃ (13–48 m² g⁻¹, Table 1) and about two folds for both the Bi₂O₃ (12–22 m² g⁻¹) and Bi₂WO₆ (27–53 m² g⁻¹), when only 3 wt% of the AC from spruce wood was added during the synthesis. Regarding the total pore volume (V_{pore}) of the materials, a similar tendency was also estimated.

From the corresponding PSDs (Fig. 3b), it is observed that the porosity of all the materials is distributed in the mesoporous range.

Table 1
Textural, chemical and optical properties for the different photocatalysts.

Sample	d_{crystal} (nm)	S _{BET} (m ² g ⁻¹)	V _{pore} (cm ³ g ⁻¹)	d_{pore} (nm)	E _g (eV)
Bi ₂ WO ₆ -a	21.6	27	0.06	4.5	3.00
Bi ₂ WO ₆ -3C-n	8.6	53	0.10	4.5, 24.0	2.94
Bi ₂ O ₃ -a	28.8	12	0.03	2.8	2.72
Bi ₂ O ₃ -3C-n	21.6	22	0.06	2.8	2.66
WO ₃ -a	21.4	13	0.03	2.9	2.73
WO ₃ -3C-a	28.6	48	0.07	2.8	2.69

d_{crystal} = crystallite size by Scherrer equation; S_{BET}= BET surface area; V_{pore}= total pore volume; d_{pore} = mean pore size; E_g= band gap.

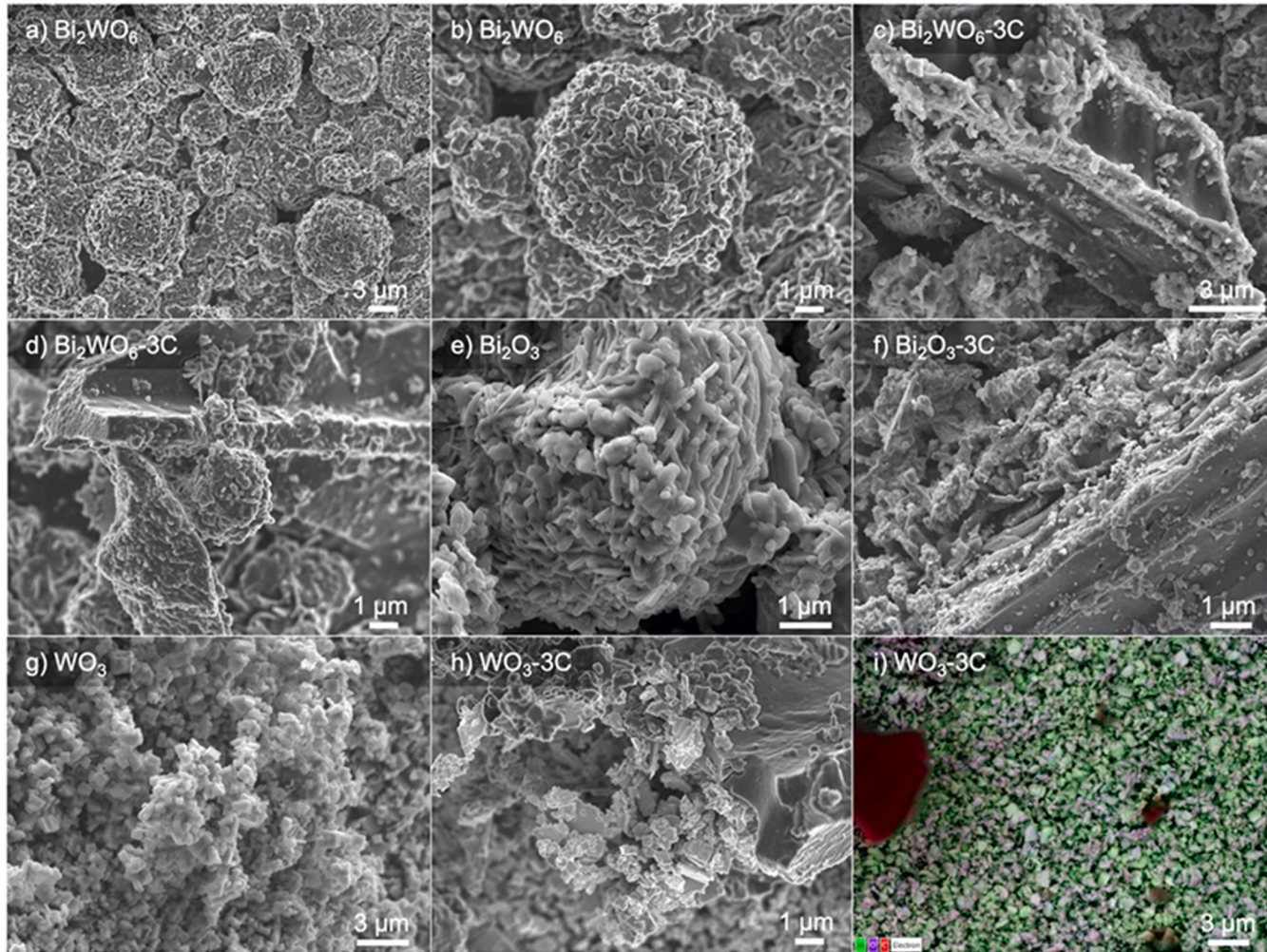


Fig. 2. SEM micrographs for the metal oxides (a, b, e, g) and their carbon-metal composites (c, d, f, h). (i) An EDX elemental mapping is also included as reference.

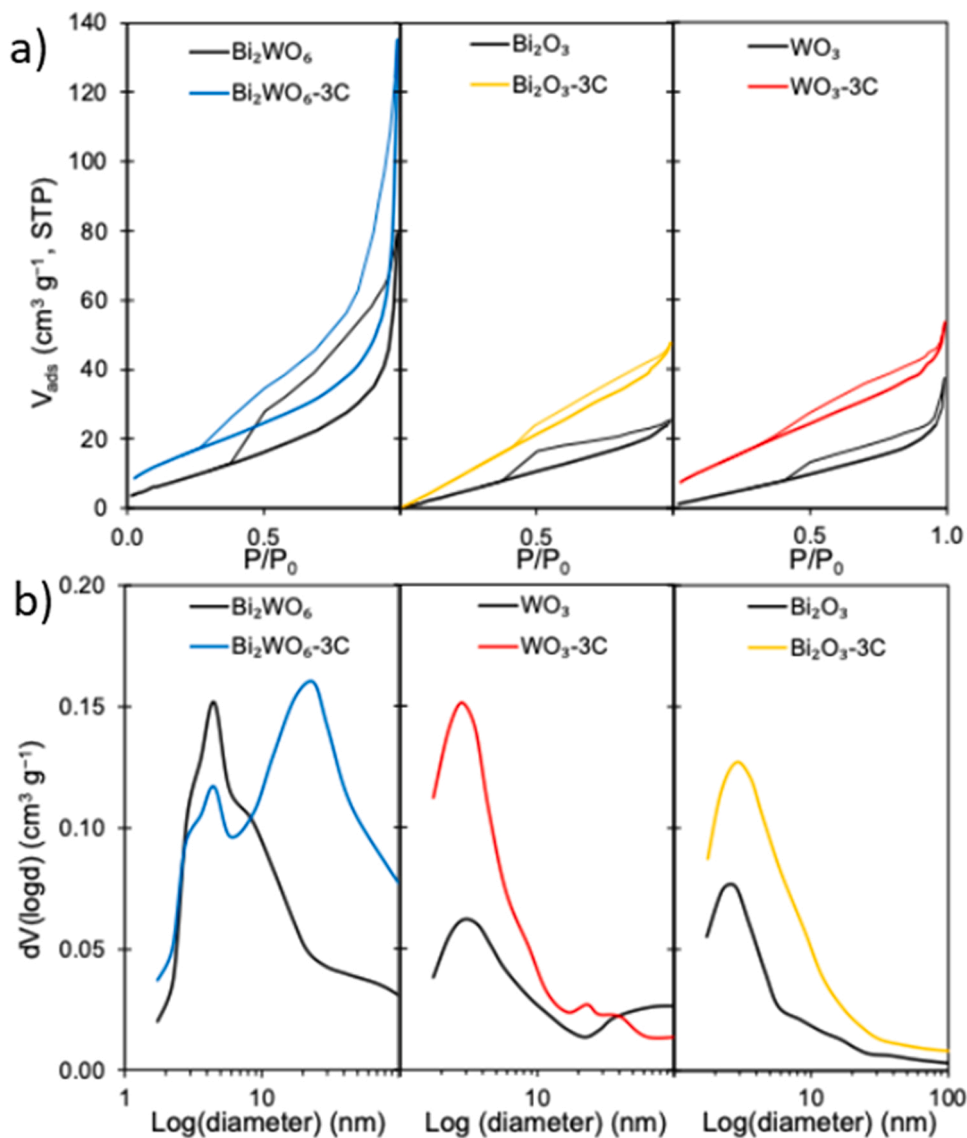


Fig. 3. (a) N_2 -adsorption-desorption isotherms and (b) pore size distribution (PSD) obtained applying BJH to the isotherm data for the different photocatalysts.

However, different pore volumes and sizes were determined depending on the type of material. Thus, PSDs determined for WO_3 , WO_3 -3C, Bi_2O_3 and Bi_2O_3 -3C were mainly monomodal ones with pore diameters between 2 and 20 nm, although some macropores ($d_{pore} > 50$ nm) were detected for WO_3 . The PSD is maintained in the same porosity range for the corresponding composites, but clearly the porosity improves in the composites, generating also a wider PSD. Bi_2WO_6 presented basically also a monomodal distribution, although more heterogeneous, however, Bi_2WO_6 -3C showed a bimodal distribution of mesopores with sizes around 4 nm and 30 nm, respectively. Otherwise, the mean pore size (d_{pore} , Table 1) was comparable for WO_3 , WO_3 -3C, Bi_2O_3 and Bi_2O_3 -3C ($d_{pore} \approx 2.8$ nm, Table 1), while a largest size of 4.5 nm for Bi_2WO_6 , and 4.5 and 24 nm for Bi_2WO_6 -3C, was calculated by applying the BJH method, corroborating that the microspheres with flower-shaped structure of Bi_2WO_6 and its composite favoured the formation of wider pores compared to the other materials.

The optical properties of the materials was studied by UV-Vis diffuse reflectance spectroscopy and the corresponding absorbance spectra in Kubelka-Munk units are depicted in Fig. 4a. For all the materials, there is a significant light absorption from the UV region extending to the visible light region, in particular for the case of the carbon-metal composites regardless the type of metal oxide used. This could be indicative of the material ability to exhibit certain photocatalytic activity under visible light irradiation. The steep curve seen in the visible light region is due to the intrinsic band gap transition (Trixy Nimmy Priscilla et al., 2024). The Tauc's plots were shown in Fig. 4b, in which the band gap of the photocatalysts slightly decreases when the carbon is added during the synthesis (Table 1). Thus, pristine WO_3 had a band gap of about 2.73 eV, which was slightly decreased to 2.69 eV for the WO_3 -3C composite. The

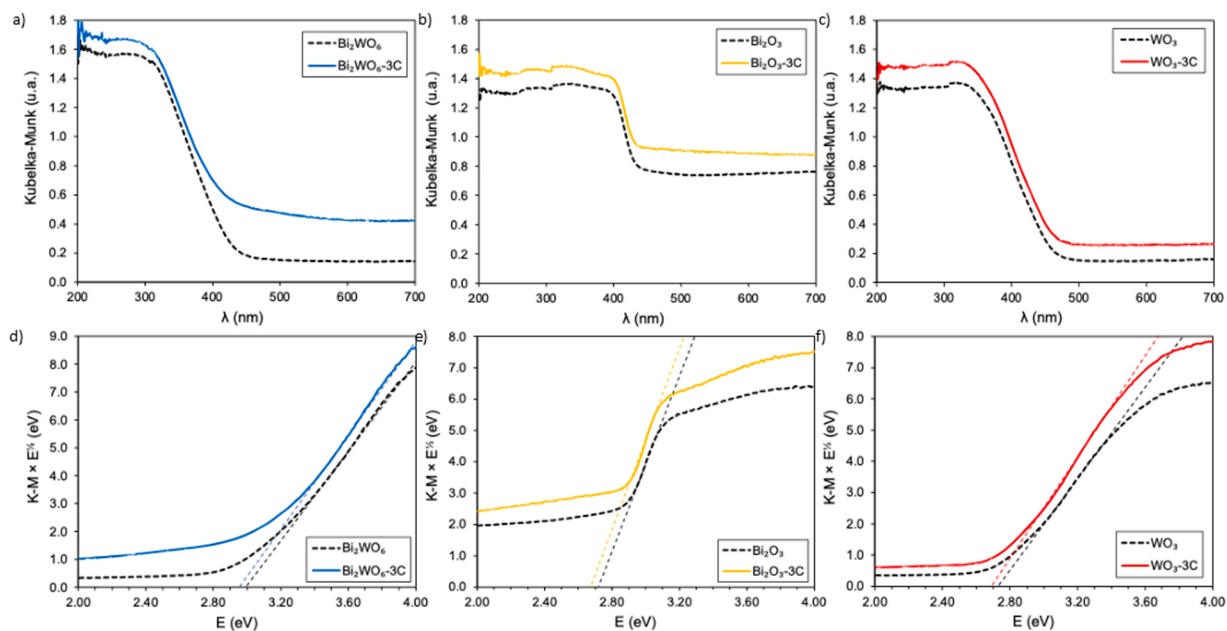


Fig. 4. (a-c) UV-Vis diffuse reflectance spectra and (d-f) Tauc's plots for the photocatalysts.

band gap of WO_3 was slightly higher than that reported in previous literature (Ketir et al., 2014; Kiamouche et al., 2022), which should be explained on the significant particle size of the nanocubes observed by SEM. The band gap of Bi_2WO_6 and Bi_2O_3 were also slightly higher than the corresponding carbon-Bi composite, and the values were within the range reported in previous works (Chen et al., 2021; Huang et al., 2020; Vijay Mane et al., 2024b). Comparing all carbon-metal composites, the band gap decreased as follows: $\text{Bi}_2\text{O}_3\text{-3C} < \text{WO}_3\text{-3C} < \text{Bi}_2\text{WO}_6\text{-3C}$. These values, between other parameters, influence on the ability of these materials to be photocatalytically active in the visible light region.

Photoluminescence (PL) spectra were recorded for metal oxides and their carbon-metal composites (Fig. 5). In general, all pure metal oxides exhibited intensive luminescence peaks due to the rapid recombination of photogenerated electron-hole pairs within the semiconductor. The faster the recombination process, the higher the fluorescence excitation intensity of the material (Zhang et al., 2019). For Bi_2WO_6 , a maximum PL emission was observed around 560 nm, while both Bi_2O_3 and WO_3 showed peaks at lower wavelengths, approximately 450 nm. The addition of carbon into the composites effectively enhanced the separation of photo-generated electron-hole pairs, as evidenced by the lower PL intensity observed for all carbon-metal composites compared to their pristine metal oxides. This suggest that the carbon phase acts as an electron acceptor, suppressing charge recombination and potentially improving the photocatalytic efficiency.

The surface chemistry of materials was investigated by XPS. The survey and the high-resolution spectra for O1s, Bi4f and W4f are shown in Fig. 6. The survey XPS spectra exhibited the typical peaks regarding the surface chemical composition of the samples (Fig. 6a). Thus, Bi_2O_3 samples presented mainly O and Bi, while Bi, W and O were detected for Bi_2WO_6 and WO_3 samples. In the case of carbon-metal composites a large amount of surface carbon was also recorded. In general, the O1s region was deconvoluted in two peaks placed at ~ 529.5 eV and ~ 530.6 corresponding to M-O bonds and chemisorbed HO/hydroxyl groups for pure metal oxides

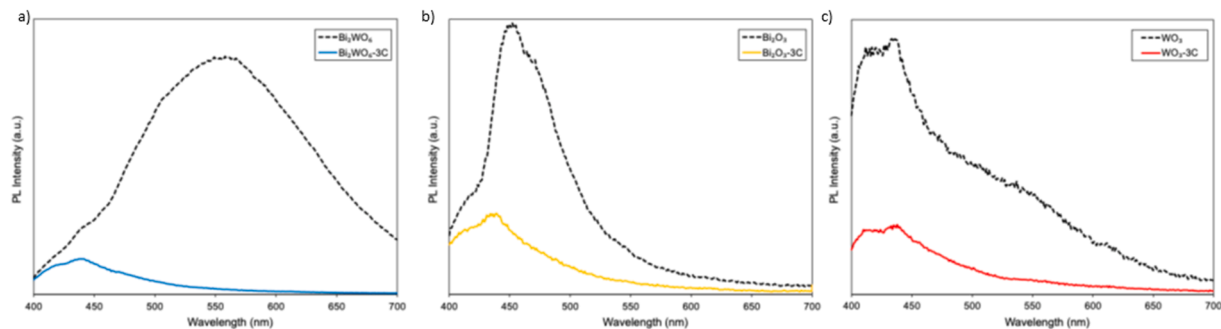


Fig. 5. Photoluminescence spectra excited at a wavelength of 370 nm for metal oxides and selected carbon-metal composites.

(Fig. 6b). In the case of carbon-metal composites, a third contribution was set at ~ 533.0 eV due to oxygenated surface groups (C–O and C=O bonds) (Madhusudan et al., 2011; Pastrana-Martínez et al., 2014). The incorporation of these oxygen functionalities was confirmed when analyzed the C1s region. Thus, three components were found (results not shown), the first one placed at ~ 284.6 eV due to C–C bonds, while the peaks at ~ 285.4 eV and ~ 288.6 eV corresponded to different oxygenated surface groups, such as hydroxyl/epoxy groups (C–O) and carbonate/carboxyl acid groups (C=O, O–C=O), respectively (Figueiredo et al., 1999). Concerning the Bi4f region, two peaks were placed at ~ 159 eV and ~ 164.3 eV with a spin-orbital splitting of 5.3 eV (Fig. 6c) attributed to the presence of Bi^{3+} in the materials. However, carbon-Bi composites showed an additional doublet at ~ 160.1 eV and ~ 165.4 eV, which should be ascribed to other Bi species with a different electronic environment favoured by the $\text{Bi}_2\text{O}_3/\text{AC}$ or $\text{Bi}_2\text{WO}_6/\text{AC}$ heterojunction (Zhu and Zhou, 2020). Finally, the W4f region was deconvoluted in two peaks placed at ~ 35.3 eV and ~ 37.5 eV with a spin-orbital splitting of ~ 2.2 eV (Fig. 6d), indicative of W^{6+} in the corresponding materials (Bi_2WO_6 and WO_3 samples and composites) (Zhu and Zhou, 2020). In this last case, no differences were observed in the spectra between the metal oxide and its corresponding carbon-metal composite.

3.2. Photocatalytic degradation of 5-FU under solar-LED irradiation

To avoid the contribution of the adsorption process on the determination of the catalytic performance of the samples, before starting the photocatalytic experiments, the aqueous solution containing the 5-FU and the photocatalyst in suspension were stirred for 30 min in the dark until reaching the adsorption equilibrium. The adsorption capacity of 5-FU was always lower than 6.7 % of the initial concentration (Fig. 7a), WO_3 and $\text{WO}_3\text{-3C}$ presenting the lowest adsorption values (< 1 %), followed by Bi_2O_3 materials and finally, Bi_2WO_6 materials. The WO_3 material had the lowest BET surface area ($13 \text{ m}^2 \text{ g}^{-1}$, Table 1), and thereby, this should explain the very low adsorption of 5-FU occurred. All carbon-metal composites presented slightly higher adsorption capacity than their corresponding metal oxides, which is indicative of an enhancement in the adsorption properties, as observed from the N_2 physisorption data (Table 1). The pollutant adsorption in aqueous solution normally is governed by the porosity of the materials and the surface chemistry (Moreno-Castilla, 2004).

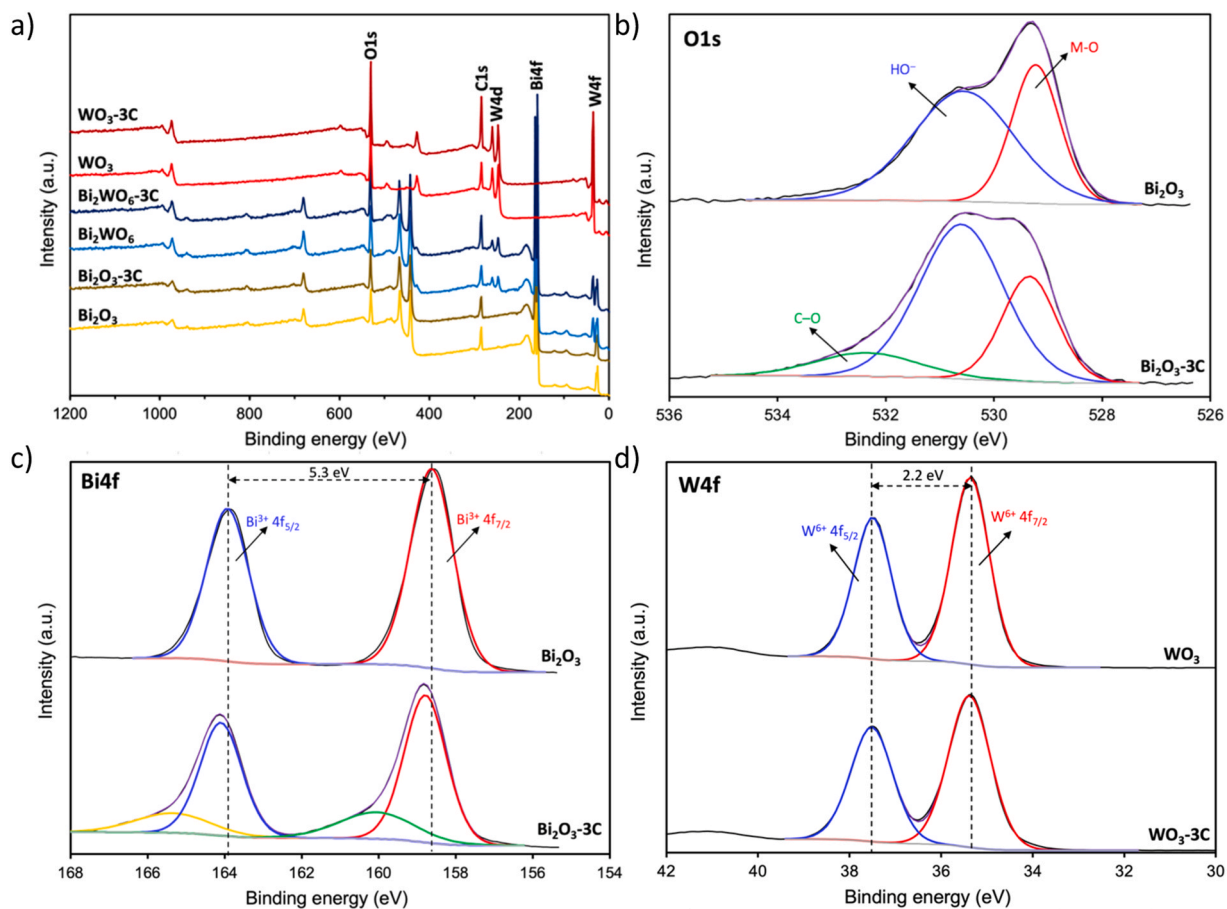


Fig. 6. XPS spectra of selected materials: (a) survey, (b) O1s, (c) Bi4f and (d) W4f. The high-resolution spectra includes the corresponding peak deconvolution.

After the dark period, the catalyst surface should be saturated allowing an adequate comparison when the materials were tested for the photodegradation of 5-FU under solar-LED irradiation (Fig. 7b-d). Initially, the photolysis of 5-FU was performed in absence of any catalyst, concluding that it was photostable under solar-LED irradiation (Fig. 7c). The 5-FU removal was consequently due to the photocatalytic performance of samples, which varied in the order: $\text{Bi}_2\text{O}_3 > \text{Bi}_2\text{WO}_6 > \text{WO}_3$ for pure semiconductors without any additional post-treatment, achieving conversion values of 68 %, 36 %, and 10 % respectively, after 100 min of reaction (Fig. 7b).

In order to establish the influence of the post-treatment on the material activity, the Bi_2WO_6 catalyst was pretreated in air ($\text{Bi}_2\text{WO}_6\text{-a}$), the results demonstrating that this thermal treatment did not influence significantly on the activity of this sample (Fig. 7c). However, the performance of all the semiconductors improved in all cases when doped with carbon and additionally, when the corresponding carbon-metal composites were post-treated in N_2 . For instance, the removal of 5-FU after 100 min of reaction was 64 % and 84 % for $\text{Bi}_2\text{WO}_6\text{-3C}$ and $\text{Bi}_2\text{WO}_6\text{-3C-n}$, respectively (Fig. 7d). The same trend of activity was found for metal-carbon composites, the most active material being that prepared with carbon and Bi_2O_3 ($\text{Bi}_2\text{O}_3\text{-3C-n}$), which was the most active photocatalyst achieving the total 5-FU conversion after 100 min. Air thermal post-treatment was also performed on the W-carbon composite ($\text{WO}_3\text{-3C-a}$), the 5-FU removal being improved from 10 % to 24 %, i.e., more than twice.

The apparent kinetic rate constant (k_{app}) and regression coefficients of the 5-FU degradation under solar-LED irradiation using all the synthesized materials are listed in Fig. 7b and Table S2, Supplementary Material. In general, a beneficial effect of the carbon added in the synthesis of the composites can be clearly observed. In all the materials, k_{app} of the metal-carbon composites is higher than the corresponding value of the pure metal oxides, suggesting that carbon adding promotes the degradation reaction. Further treatments with nitrogen increased the reaction kinetics and complete removal was achieved at a lower time. Hence, there is a combination of the effect of carbon and further treatment in both efficiency and kinetics. In all materials as well, the presence of carbon provokes an increase in the specific surface area and pore volume of the respective semiconductors. Porosity and specific surface area have been reported to play an important role in photodegradation reactions (Ketir et al., 2014; Leary and Westwood, 2011). Furthermore, the

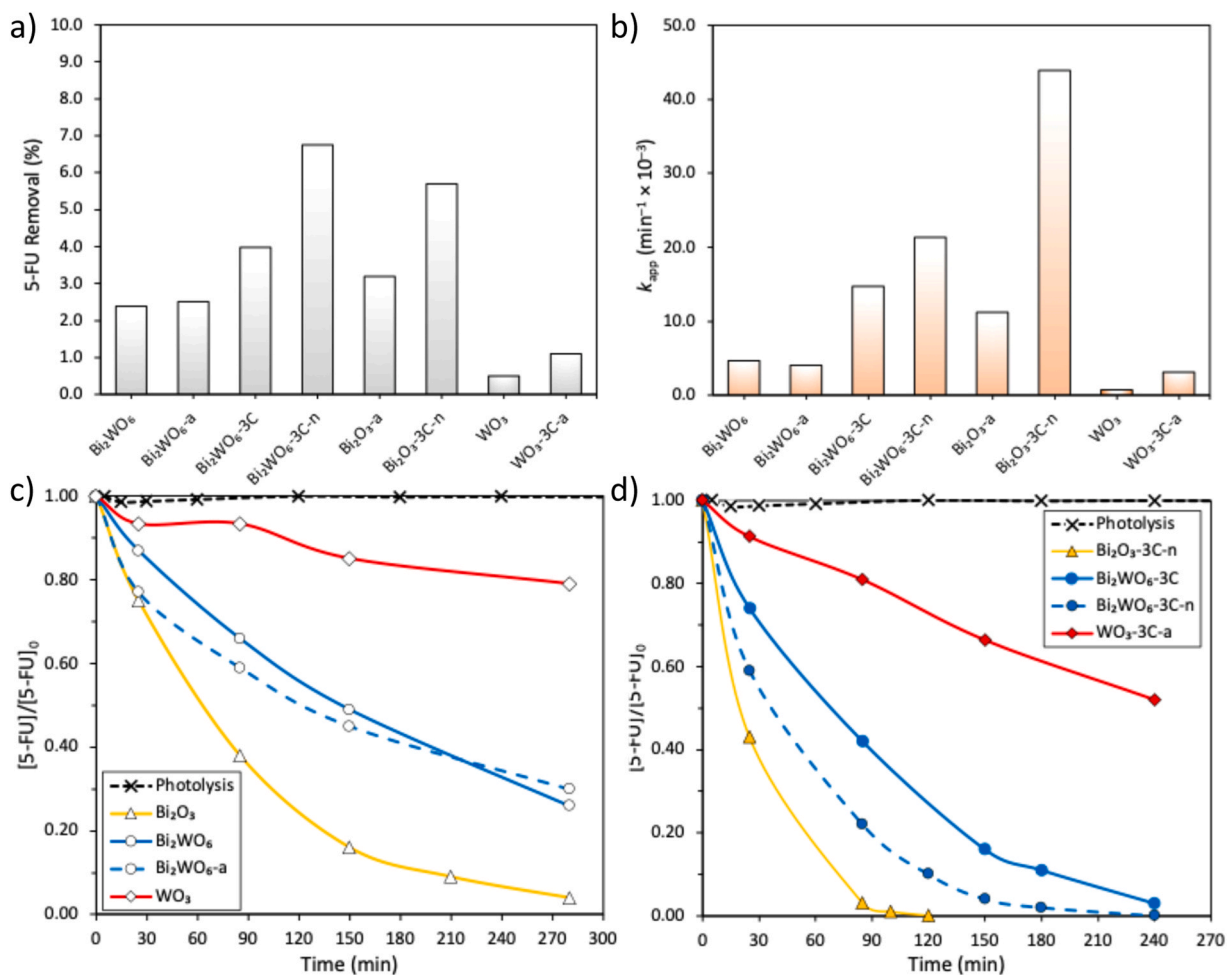


Fig. 7. 5-FU removal obtained (a) by adsorption during the dark phase, and the photocatalytic process using (c) pure semiconductors and (d) carbon-metal composites; (b) Apparent kinetic rate constant (k_{app}) from photocatalytic reaction data. (Bi_2WO_6 refers to the material after the hydrothermal synthesis).

Table 2
Survey literature of different photocatalysts used for the removal of 5-FU in water.

Material	Removal (%) / time (min)	5-FU concentration (mg L ⁻¹) / catalyst loading (g L ⁻¹)	Irradiation type	Reference
g-C ₃ N ₄	99/30	10/1	Medium pressure Hg lamp (λ > 350 nm)	(Pérez-Molina et al., 2023)
g-C ₃ N ₄	55/420	10/1	Solar-LED (λ > 410 nm)	(Pérez-Molina et al., 2023)
g-CN/Ni ₃ (VO ₄) ₂ /ZnCr ₂ O ₄	100/200	20/0.02	Halogen lamp (λ > 200 nm)	(Swedha et al., 2022)
g-CNQDs/ CuFe ₂ O ₄ /Cu ⁰	100/60	3.9/0.2	Xe lamp (λ > 420 nm)	(Wang et al., 2023)
g-C ₃ N ₄ /ZnO	100/180	20/1	UV-LED (λ = 385 nm)	(Pérez-Molina et al., 2022)
BiOCl	100/60	15/0.2	Medium pressure Hg lamp (λ > 200 nm)	(Wilczewska and Bielicka-gieldo, 2021)
BiOClBr	100/90	15/0.5	Medium pressure Hg lamp (λ > 200 nm)	(Wilczewska et al., 2019)
P25	100/120	0.2/0.005	UV lamp (λ > 254 nm)	(Lin and Lin, 2014)
Bi-B doped TiO ₂	95/240	50/0.25	Xe lamp (λ > 420 nm)	(Fiszka Borzyszkowska et al., 2016)
N/S doped TiO ₂	80/180	10/0.1	Xe lamp (λ > 300 nm)	(Koltsakidou et al., 2017)
TiO ₂ -TBMA	100/180	15/0.5	Xe lamp (λ > 420 nm)	(Wilczewska et al., 2022)
	100/60	15/0.5	Medium pressure Hg lamp (λ _{max} = 366 nm)	
PET-10 wt% TiO ₂	94/360	1/1	Xe lamp (λ > 300 nm)	(Evgenidou et al., 2020)
PLLA-GO-10 wt% TiO ₂	40/360	1/1	Xe lamp (λ > 300 nm)	
		5/1	Solar-LED (λ > 380 nm)	This study
WO ₃ -C	75/420			
Bi ₂ O ₃ -C	100/100			
Bi ₂ WO ₆ -C	100/180			

g-C₃N₄: graphitic carbon nitride; g-CNQDs: graphitic carbon nitride quantum dots; TBMA: tributylmethylammonium chloride; PET: Poly(ethylene terephthalate); PLLA-GO: poly(L-lactic acid)-graphene oxide.

performance of these materials is also linked to their physico-chemical properties, and this explains the order in activity. Typically, smaller crystallite sizes correspond to an increased number of surface defects providing more active sites for photocatalytic reactions (Wang et al., 2014). However, Nandiyanto et al.,(2020) (Nandiyanto et al., 2020) reported that in the case of monoclinic WO₃, the increase in crystallite size had a positive correlation on its photocatalytic activity. This could explain why, WO₃-3C firstly with a crystallite size of 28.6 nm, performed better than WO₃ with a 21.4 nm crystal size. In addition, its high specific surface area as well compared to that for WO₃ added to the improved efficiency. However, as earlier mentioned, the carbon in the WO₃-3C material seems to not be well integrated with the WO₃ nanocubes, hence the impact of carbon was less compared to the Bi-based materials, as the odds were high that the particles used during the experiments did not have a homogenous distribution of carbon. In the case of Bi-based materials, the smallest crystallite size for Bi₂WO₆-3C led to the highest specific surface area and provided more active sites for photocatalysis. Despite these, its efficiency and kinetics were lower than those of Bi₂O₃ and its composite. This could be explained by its wider band gap, since Bi₂O₃ and its composite had band gaps of about 0.3 eV lower than that for Bi₂WO₆ and Bi₂WO₆-3C, making them more active under the solar-LED irradiation. It can be inferred from literature that the presence of the carbon phase favours the separation of photogenerated carriers leading to charge transfer reactions. The carbon increases the number of photogenerated holes and electrons compared to the bare metal oxides, hence increasing photocatalytic activity. Carbonaceous structures are known to have high conductivity, promote charge transfer, enable better separation of electron-hole pairs, improve surface reactivities hence delaying their recombination (Elaoui et al., 2023; Q. Ma et al., 2022; Zhao et al., 2015). From the rate constant values, the highest performance was obtained for Bi₂WO₆-3C-N₂ and Bi₂O₃-3C-N₂ treated in nitrogen, and bismuth oxides without treatment.

Table 2 summarizes some studies regarding the recently works published for the removal of 5-FU in water. It is worthwhile noting that the experimental parameters such as catalyst loading, pollutant concentration and most especially light irradiation source differ making it challenging to do an accurate comparison. However, it can be observed that the photocatalysts prepared in this work, especially the composites showed an excellence photoactivity for the degradation of 5-FU under solar-LED irradiation compared to the materials reported in literature under similar light irradiation and even, irradiations of higher energy and intensity.

4. Conclusions

Tungsten and bismuth-based photocatalysts and their carbon-metal composites were prepared under same hydrothermal conditions and with a different post-treatment in nitrogen or air atmosphere to ascertain which further treatment was better for the functionality of the materials. The materials were thoroughly characterized and used as photocatalysts for the degradation of 5-FU in water under solar-LED irradiation. The morphology and structure of the materials depended on the type of semiconductor synthesized.

Thus, Bi₂O₃ was composed by worm-like structures, while elongated particles forming microspheres and nanocube particles were observed for Bi₂WO₆ and for WO₃, respectively. The carbon-metal composites showed a well-integrated carbon grains coated by the metal oxide particles, especially in the case of Bi-carbon composites. In addition, the presence of carbon provoked an increase in the specific surface area and pore volume, a reduced band gap and lower crystallite size compared to the original semiconductor. The xps analysis confirmed the incorporation of the carbon functionalities in the composites while the PL spectra showed that the carbon phase in the composites contributed to a lower intensity suggesting a suppression in charge recombination in the composites. Regarding the photocatalytic performance, all materials were active for the 5-FU removal under solar-LED irradiation, Bi-based materials, i.e., Bi₂O₃ and Bi₂WO₆, being more active than WO₃, as well as the corresponding carbon-metal composites showed a superior activity compared to the original semiconductor. The influence of the post-treatment on the activity depended on the type of semiconductor tested. Thus, air thermal post-treatment did not seem to affect significantly on the activity of Bi₂WO₆. However, the nitrogen post-treatment improved remarkably the efficiency of all Bi-carbon composites. In the case of WO₃ materials, air post-treatment favoured the activity of the materials because a higher crystallite size was obtained. In all materials, the presence of carbon improves the reaction kinetic rates and overall efficiency irrespective of the semiconductor used. Overall, total photodegradation of 5-FU was obtained using Bi₂O₃-3C-n in 100 mins, followed of Bi₂WO₆-3C-n in 240 mins and finally, WO₃-3C-a in 420 mins. This work therefore establishes novel information on the further treatment, which improves the structure and performance of the Bi-based photocatalysts for their application in wastewater treatment of resistant organic pollutants and other environmental remediation studies.

CRedit authorship contribution statement

Velma Beri Kimbi Yaah: Conceptualization, Methodology, Validation, Formal analysis, Investigation, Writing - original draft, Writing - review & editing, Funding acquisition. **L.M. Pastrana-Martínez:** Conceptualization, Methodology, Validation, Writing - review & editing. **F.J. Maldonado-Hódar:** Conceptualization, Validation, Writing - review & editing. **S. Morales-Torres:** Conceptualization, Investigation, Data curation, Resources, Writing - review & editing, Supervision.

Declaration of Competing Interest

The authors declare that they have no known competing financial interests or personal relationships that could have appeared to influence the work reported in this paper.

Acknowledgements

This work was financially supported by Junta de Andalucía – Conserjería de Universidad, Investigación e Innovación – Project P21_00208 and by project PID2021–126579OB-C31 from MCIN/AEI/10.13039/501100011033 and “ERDF A way of making Europe”. VBKY acknowledges the Finnish Foundation for Technology promotion, tekniikan edistämissäätiö and Soroptimist International Europe (SIE). SMT is grateful to MICIN/AEI/10.13039/501100011033 and FSE “El FSE invierte en tu futuro” for his Ramon y Cajal research contract (RYC-2019–026634-I). “Unidad de Excelencia Química Aplicada a Biomedicina y Medioambiente” of the University of Granada (UEQ-UGR) is gratefully acknowledged for the technical assistance.

Appendix A. Supporting information

Supplementary data associated with this article can be found in the online version at [doi:10.1016/j.eti.2025.104148](https://doi.org/10.1016/j.eti.2025.104148).

Data availability

Data will be made available on request.

References

- Ahmad, K., Nde, D.T., Khan, R.A., 2024. Hydrothermal synthesis of bismuth-doped tungsten trioxide (Bi-WO₃) for photocatalytic hydrogen production application. *React. Kinet. Mech. Catal.* <https://doi.org/10.1007/s11444-024-02679-x>.
- Balzer, R., Drago, V., Schreiner, W.H., Probst, L.F.D., 2014. Synthesis and structure-activity relationship of a WO₃ catalyst for the total oxidation of BTX. *J. Braz. Chem. Soc.* 25, 2026–2031. <https://doi.org/10.5935/0103-5053.20140187>.
- Barrett, E.P., Joyner, L.G., Halenda, P.P., 1951. The determination of pore volume and area distributions in porous substances. I. Computations from nitrogen isotherms. *J. Am. Chem. Soc.* 73, 373–380. <https://doi.org/10.1021/ja01145a126>.
- Bayahia, H., 2022. Green synthesis of activated carbon doped tungsten trioxide photocatalysts using leaf of basil (*Ocimum basilicum*) for photocatalytic degradation of methylene blue under sunlight. *J. Saudi Chem. Soc.* 26, 101432. <https://doi.org/10.1016/j.jscs.2022.101432>.
- Brunauer, S., Emmett, P.H., Teller, E., 1938. Adsorption of gases in multimolecular layers. *J. Am. Chem. Soc.* 60, 309–319. <https://doi.org/10.1021/ja01269a023>.
- Bu, E., Chen, X., López-Cartes, C., Cazaña, F., Monzón, A., Martínez-López, J., Delgado, J.J., 2023. Effect of the TiO₂-carbon interface on charge transfer and ethanol photo-reforming. *Catal. Today* 422, 114220. <https://doi.org/10.1016/j.cattod.2023.114220>.
- Chen, Lili, Xu, B., Jin, M., Chen, Lunjian, Yi, G., Xing, B., Zhang, Y., Wu, Y., Li, Z., 2023. Excellent photocatalysis of Bi₂WO₆ structured with oxygen vacancies in degradation of tetracycline. *J. Mol. Struct.* 1278, 134911. <https://doi.org/10.1016/j.molstruc.2023.134911>.

- Chen, T., Liu, L., Hu, C., Huang, H., 2021. Recent advances on Bi₂WO₆-based photocatalysts for environmental and energy applications. *Chin. J. Catal.* 42, 1413–1438. [https://doi.org/10.1016/S1872-2067\(20\)63769-X](https://doi.org/10.1016/S1872-2067(20)63769-X).
- Crowley, L.C., Marfell, B.J., Scott, A.P., Waterhouse, N.J., 2016. Triggering apoptosis in hematopoietic cells with cytotoxic drugs. *Cold Spring Harb. Protoc.* 2016. <https://doi.org/10.1101/pdb.prot087130>.
- Elaloui, A., El Ouardi, M., BaQais, A., Arab, M., Saadi, M., Ait Ahsaine, H., 2023. Bismuth tungstate Bi₂WO₆: a review on structural, photophysical and photocatalytic properties. *RSC Adv.* 13, 17476–17494. <https://doi.org/10.1039/D3RA01987J>.
- Evgenidou, E., Ofrydopoulou, A., Malesic-Elfeheriadou, N., Nannou, C., Ainali, N.M., Christodoulou, E., Bikiaris, D.N., Kyzas, G.Z., Lambropoulou, D.A., 2020. New insights into transformation pathways of a mixture of cytostatic drugs using Polyester-TiO₂ films: Identification of intermediates and toxicity assessment. *Sci. Total Environ.* 741, 140394. <https://doi.org/10.1016/j.scitotenv.2020.140394>.
- Feng, M., Qu, R., Zhang, X., Sun, P., Sui, Y., Wang, L., Wang, Z., 2015. Degradation of flumequine in aqueous solution by persulfate activated with common methods and polyhydroquinone-coated magnetite/multi-walled carbon nanotubes catalysts. *Water Res.* 85, 1–10. <https://doi.org/10.1016/j.watres.2015.08.011>.
- Figueiredo, J.L., Pereira, M.F.R., Freitas, M.M.A., Órfão, J.J.M., 1999. Modification of the surface chemistry of activated carbons. *Carbon N. Y.* 37, 1379–1389. [https://doi.org/10.1016/S0008-6223\(98\)00333-9](https://doi.org/10.1016/S0008-6223(98)00333-9).
- Fiszka Borzyszkowska, A., Pieczyńska, A., Ofiarska, A., Nikiforow, K., Stepnowski, P., Siedlecka, E.M., 2016. Bi-B-TiO₂-based photocatalytic decomposition of cytostatic drugs under simulated sunlight treatments. *Sep. Purif. Technol.* 169, 113–120. <https://doi.org/10.1016/j.seppur.2016.06.012>.
- Ganzenko, O., Oturan, N., Sirés, I., Huguenot, D., van Hullebusch, E.D., Esposito, G., Oturan, M.A., 2018. Fast and complete removal of the 5-fluorouracil drug from water by electro-Fenton oxidation. *Environ. Chem. Lett.* 16, 281–286. <https://doi.org/10.1007/s10311-017-0659-6>.
- Gomis-Berenguer, A., Eliani, I., F. Lourenço, V., J. Carmona, R., F. Velasco, L., O. Ania, C., 2019. Insights on the use of carbon additives as promoters of the visible-light photocatalytic activity of Bi₂WO₆. *Materials* 12. <https://doi.org/10.3390/ma12030385>.
- Gui, M.-S., Zhang, W.-D., 2011. Preparation and modification of hierarchical nanostructured Bi₂WO₆ with high visible light-induced photocatalytic activity. *Nanotechnology* 22, 265601. <https://doi.org/10.1088/0957-4484/22/26/265601>.
- Huang, H., Zhao, J., Du, Y., Zhou, C., Zhang, M., Wang, Z., Weng, Y., Long, J., Hofkens, J., Steele, J.A., Roeyfaers, M.B.J., 2020. Direct Z-scheme heterojunction of semicoherent FAPbBr₃/Bi₂WO₆ interface for photoredox reaction with large driving force. *ACS Nano* 14, 16689–16697. <https://doi.org/10.1021/acsnano.0c03146>.
- Jureczko, M., Kalka, J., 2020. Cytostatic pharmaceuticals as water contaminants. *Eur. J. Pharmacol.* 866, 172816. <https://doi.org/10.1016/j.ejphar.2019.172816>.
- Karen, V.G., Hernández-Gordillo, A., Oros-Ruiz, S., Rodil, S.E., 2021. Microparticles of α-Bi₂O₃ obtained from bismuth basic nitrate [Bi₆O₆(OH)₂(NO₃)₄·2H₂O] with photocatalytic properties. *Top. Catal.* 64, 121–130. <https://doi.org/10.1007/s11244-020-01299-8>.
- Ketir, W., Trari, M., Bessekhouad, Y., 2014. Visible light induced HCl splitting over the hetero-system p-CuCrO₂/n-WO₃. *Renew. Energy* 69, 1–6. <https://doi.org/10.1016/j.renene.2014.03.021>.
- Kiamouche, S., Messaadia, L., Lahmar, H., Rekhila, G., Trari, M., Benamira, M., 2022. Enhanced photocatalytic degradation of Ponceau S Red dye in the novel hetero-system Fe₂O₃/WO₃ under solar light irradiation. *React. Kinet. Mech. Catal.* 135, 3411–3426. <https://doi.org/10.1007/s11144-022-02313-8>.
- Koltsakidou, A., Antonopoulou, M., Evgenidou, E., Konstantinou, I., Giannakas, A.E., Papadaki, M., Bikiaris, D., Lambropoulou, D.A., 2017. Photocatalytic removal of fluorouracil using TiO₂-P25 and N/S doped TiO₂ catalysts: A kinetic and mechanistic study. *Sci. Total Environ.* 578, 257–267. <https://doi.org/10.1016/j.scitotenv.2016.08.208>.
- Leary, R., Westwood, A., 2011. Carbonaceous nanomaterials for the enhancement of TiO₂ photocatalysis. *Carbon N. Y.* 49, 741–772. <https://doi.org/10.1016/j.carbon.2010.10.010>.
- Lin, H.H.-H., Lin, A.Y.-C., 2014. Photocatalytic oxidation of 5-fluorouracil and cyclophosphamide via UV/TiO₂ in an aqueous environment. *Water Res.* 48, 559–568. <https://doi.org/10.1016/j.watres.2013.10.011>.
- Lutterbeck, C.A., Wilde, M.L., Baginska, E., Leder, C., Machado, É.L., Kümmerer, K., 2016. Degradation of cyclophosphamide and 5-fluorouracil by UV and simulated sunlight treatments: Assessment of the enhancement of the biodegradability and toxicity. *Environ. Pollut.* 208, 467–476. <https://doi.org/10.1016/j.envpol.2015.10.016>.
- Ma, J., Zhao, B., Fan, X., Wang, W., Chen, X., Shao, N., Jiang, P., 2022. Ag/rGO/Bi₂WO₆ nanocomposite as a highly efficient and stable photocatalyst for Rhodamine B degradation under visible light irradiation. *Diam. Relat. Mater.* 127, 109143. <https://doi.org/10.1016/j.diamond.2022.109143>.
- Ma, Q., Song, R., Ren, F., Wang, H., Gao, W., Li, Z., Li, C., 2022. Photoelectrocatalytic degradation of refractory pollutants over WO₃/W network photoelectrode with heterophase junction for enhancing mass transportation and charge separation. *Appl. Catal. B Environ.* 309, 121292. <https://doi.org/10.1016/j.apcatb.2022.121292>.
- Madhusudan, P., Ran, J., Zhang, J., Yu, J., Liu, G., 2011. Novel urea assisted hydrothermal synthesis of hierarchical BiVO₄/Bi₂O₂CO₃ nanocomposites with enhanced visible-light photocatalytic activity. *Appl. Catal. B Environ.* 110, 286–295. <https://doi.org/10.1016/j.apcatb.2011.09.014>.
- Majumdar, S., Nag, P., Devi, P.S., 2014. Enhanced performance of CNT/SnO₂ thick film gas sensors towards hydrogen. *Mater. Chem. Phys.* 147, 79–85. <https://doi.org/10.1016/j.matchemphys.2014.04.009>.
- Mane, V.A., Dake, D.V., Raskar, N.D., Sonpir, R.B., Stathatos, E., Dole, B.N., 2023. Magneto-optical properties of Fe-doped bismuth oxide nanorods for photocatalytic and antimicrobial applications. *Results Chem.* 6, 101083. <https://doi.org/10.1016/j.rechem.2023.101083>.
- Mane, V.A., Dake, D.V., Raskar, N.D., Sonpir, R.B., Stathatos, E., Dole, B.N., 2024c. Growth in defects and surface area for the photocatalytic performance of GO-based Fe-doped bismuth oxide mesoporous nanocomposite. *Ceram. Int.* 50, 11179–11189. <https://doi.org/10.1016/j.ceramint.2024.01.019>.
- Mane, Vijay, Dake, D., Raskar, N., Sonpir, R., Stathatos, E., Dole, B., 2024a. A review on Bi₂O₃ nanomaterial for photocatalytic and antibacterial applications. *Chem. Phys. Impact* 8, 100517. <https://doi.org/10.1016/j.chphi.2024.100517>.
- Mane, Vijay A., Dake, D.V., Raskar, N.D., Sonpir, R.B., Dole, B.N., 2024b. Synergistic enhancement of photocatalytic and antifungal activities in microwave-assisted ZnO/Fe-doped Bi₂O₃ nanocomposites. *Phys. Status Solidi Appl. Mater. Sci.* 221, 1–14. <https://doi.org/10.1002/pssa.202300954>.
- Morales-Torres, S., Pastrana-Martínez, L.M., Figueiredo, J.L., Faria, J.L., Silva, A.M.T., 2012. Design of graphene-based TiO₂ photocatalysts—a review. *Environ. Sci. Pollut. Res.* 19, 3676–3687. <https://doi.org/10.1007/s11356-012-0939-4>.
- Moreno-Castilla, C., 2004. Adsorption of organic molecules from aqueous solutions on carbon materials. *Carbon N. Y.* 42, 83–94. <https://doi.org/10.1016/j.carbon.2003.09.022>.
- Murcia-López, S., Navío, J.A., Hidalgo, M.C., 2013. Role of activated carbon on the increased photocatalytic activity of AC/Bi₂WO₆ coupled materials. *Appl. Catal. A Gen.* 466, 51–59. <https://doi.org/10.1016/j.apcata.2013.06.022>.
- Muruganandham, M., Amutha, R., Lee, G.-J., Hsieh, S.-H., Wu, J.J., Sillanpää, M., 2012. Facile fabrication of tunable Bi₂O₃ self-assembly and its visible light photocatalytic activity. *J. Phys. Chem. C* 116, 12906–12915. <https://doi.org/10.1021/jp302343f>.
- Nandiyanto, A.B.D., Zaen, R., Oktiani, R., 2020. Correlation between crystallite size and photocatalytic performance of micrometer-sized monoclinic WO₃ particles. *Arab. J. Chem.* 13, 1283–1296. <https://doi.org/10.1016/j.arabjc.2017.10.010>.
- Narayanan, V., Mandal, B.K., 2023. Type-II ternary Bi₂WO₆/rGO/SnFe₂O₄ heterojunction nanocomposites and their photocatalytic efficiency towards 4-nitrophenol reduction. *RSC Adv.* 13, 22616–22629. <https://doi.org/10.1039/D3RA03647B>.
- Pastrana-Martínez, L.M., Morales-Torres, S., Likodimos, V., Figueiredo, J.L., Faria, J.L., Falaras, P., Silva, A.M.T., 2012. Advanced nanostructured photocatalysts based on reduced graphene oxide-TiO₂ composites for degradation of diphenhydramine pharmaceutical and methyl orange dye. *Appl. Catal. B Environ.* 123–124, 241–256. <https://doi.org/10.1016/j.apcatb.2012.04.045>.
- Pastrana-Martínez, L.M., Morales-Torres, S., Likodimos, V., Falaras, P., Figueiredo, J.L., Faria, J.L., Silva, A.M.T., 2014. Role of oxygen functionalities on the synthesis of photocatalytically active graphene-TiO₂ composites. *Appl. Catal. B Environ.* 158–159, 329–340. <https://doi.org/10.1016/j.apcatb.2014.04.024>.
- Pérez-Molina, A., Pastrana-Martínez, L.M., Pérez-Poyatos, L.T., Morales-Torres, S., Maldonado-Hódar, F.J., 2022. One-pot thermal synthesis of g-C₃N₄/ZnO composites for the degradation of 5-fluorouracil cytostatic drug under UV-LED irradiation. *Nanomaterials* 12. <https://doi.org/10.3390/nano12030340>.
- Pérez-Molina, A., Pastrana-Martínez, L.M., Morales-Torres, S., Maldonado-Hódar, F.J., 2023. Photodegradation of cytostatic drugs by g-C₃N₄: synthesis, properties and performance fitted by selecting the appropriate precursor. *Catal. Today* 418, 114068. <https://doi.org/10.1016/j.cattod.2023.114068>.

- Priya, R., Raman, M.S., Kumar, N.S., Chandrasekaran, J., Balan, R., 2016. Synthesis and characterization of CTAB-assisted WO₃ deposited on silicon for the fabrication of photoresponse p-n junction diode. *Opt. (Stuttg.)* 127, 7913–7924. <https://doi.org/10.1016/j.ijleo.2016.05.072>.
- Raza, W., Ahmad, K., 2022. Graphitic carbon nitride-based photocatalysts for hydrogen production. *Sustain. Mater. Green. Process. Energy Convers.* 213–236. <https://doi.org/10.1016/B978-0-12-822838-8.00003-X>.
- Regadera-Macías, A.M., Morales-Torres, S., Pastrana-Martínez, L.M., Maldonado-Hódar, F.J., 2024. Optimizing filters of activated carbons obtained from biomass residues for ethylene removal in agro-food industry devices. *Environ. Res.* 248, 118247. <https://doi.org/10.1016/j.envres.2024.118247>.
- Rhoomi, Z.R., Ahmed, D.S., Jabir, M.S., Qadeer, A., Ismael, A.B., Swelum, A.A., 2024. Fabrication of pure Bi₂WO₆ and Bi₂WO₆/MWCNTs nanocomposite as potential antibacterial and anticancer agents. *Sci. Rep.* 14, 9545. <https://doi.org/10.1038/s41598-024-58751-y>.
- Sing, K.S.W., 1985. Reporting physisorption data for gas/solid systems with special reference to the determination of surface area and porosity. *Pure Appl. Chem.* 57, 603–619.
- Swedha, M., Alatar, A.A., Okla, M.K., Alaraidh, I.A., Mohebalain, A., Aufy, M., Raju, L.L., Thomas, A.M., Abdel-Maksoud, M.A., Sudheer Khan, S., 2022. Graphitic carbon nitride embedded Ni₃(VO₄)₂/ZnCr₂O₄ Z-scheme photocatalyst for efficient degradation of p-chlorophenol and 5-fluorouracil, and genotoxic evaluation in Allium cepa. *J. Ind. Eng. Chem.* 112, 244–257. <https://doi.org/10.1016/j.jiec.2022.05.018>.
- Thommes, M., Kaneko, K., Neimark, A.V., Olivier, J.P., Rodríguez-Reinoso, F., Rouquerol, J., Sing, K.S.W., 2015. Physisorption of gases, with special reference to the evaluation of surface area and pore size distribution (IUPAC Technical Report). *Pure Appl. Chem.* 87, 1051–1069. <https://doi.org/10.1515/pac-2014-1117>.
- Trixy Nimmy Priscilla, D., Radha, R., Chitra, A., Geetha, S.K., 2024. Comprehensive Evaluation of Nanosized Bismuth Tungstate (Bi₂WO₆) as Photoanodes for Photoelectrochemical Water Splitting Performance. *J. Clust. Sci.* 35, 875–889. <https://doi.org/10.1007/s10876-023-02520-w>.
- Wang, A., Guo, S., Xu, M., Meng, C., Zhu, H., Zheng, T., Wang, H., Wang, K., Shi, W., Liu, X., Song, X., Chang, Z., 2023. OD/3D CNQDs/CuFe₂O₄/Cu₀ heterostructures as broad spectrum photocatalyst for efficient 5-fluorouracil degradation: Structural evolution and relay oxidation process. *Appl. Catal. B Environ.* 322, 122117. <https://doi.org/10.1016/j.apcatb.2022.122117>.
- Wang, L., Hu, H., Xu, J., Zhu, S., Ding, A., Deng, C., 2019. WO₃ nanocubes: Hydrothermal synthesis, growth mechanism, and photocatalytic performance. *J. Mater. Res.* 34, 2955–2963. <https://doi.org/10.1557/jmr.2019.189>.
- Wang, X., Sø, L., Su, R., Wendt, S., Hald, P., Mamakhel, A., Yang, C., Huang, Y., Iversen, B.B., Besenbacher, F., 2014. The influence of crystallite size and crystallinity of anatase nanoparticles on the photo-degradation of phenol. *J. Catal.* 310, 100–108. <https://doi.org/10.1016/j.jcat.2013.04.022>.
- Wilczewska, P., Bielicka-gieldo, A., 2021. Morphology regulation mechanism and enhancement of. *Catalysts* 11, 1–20.
- Wilczewska, P., Bielicka-Gieldo, A., Borzyszkowska, A.F., Ryl, J., Klimczuk, T., Siedlecka, E.M., 2019. Photocatalytic activity of solvothermal prepared BiOClBr with imidazolium ionic liquids as a halogen sources in cytostatic drugs removal. *J. Photochem. Photobiol. A Chem.* 382, 111932. <https://doi.org/10.1016/j.jphotochem.2019.111932>.
- Wilczewska, P., Pancielejko, A., Łuczak, J., Kroczevska, M., Lisowski, W., Siedlecka, E.M., 2022. The influence of ILs on TiO₂ microspheres activity towards 5-FU removal under artificial sunlight irradiation. *Appl. Surf. Sci.* 573, 151431. <https://doi.org/10.1016/j.apsusc.2021.151431>.
- Yang, S., Cao, J., Xu, W., He, X., Wang, Z., Zhang, Z., Sun, Z., Zhang, H., Wang, S., 2022. Controlling the crystal phase structure of WO₃ nanosheet-based hierarchical spheres for enhanced gas sensing performance. *ACS Appl. Nano Mater.* 5, 16544–16552. <https://doi.org/10.1021/acsnm.2c03178>.
- Zhang, R., Zhang, T., Zhao, C., 2019. A novel Z-scheme Bi₂WO₆-based photocatalyst with enhanced dye degradation activity. *Nanopart. Res Springe Nat.*
- Zhao, Q., Gong, M., Liu, W., Mao, Y., Le, S., Ju, S., Long, F., Liu, X., Liu, K., Jiang, T., 2015. Enhancement of visible-light photocatalytic activity of silver and mesoporous carbon co-modified Bi₂WO₆. *Appl. Surf. Sci.* 332, 138–146. <https://doi.org/10.1016/j.apsusc.2015.01.122>.
- Zhu, D., Zhou, Q., 2020. Novel Bi₂WO₆ modified by N-doped graphitic carbon nitride photocatalyst for efficient photocatalytic degradation of phenol under visible light. *Appl. Catal. B Environ.* 268, 118426. <https://doi.org/10.1016/j.apcatb.2019.118426>.